RSC Applied Interfaces

ROYAL SOCIETY OF CHEMISTRY

PAPER

View Article Online
View Journal | View Issue

Cite this: *RSC Appl. Interfaces*, 2025, **2**, 1829

Biogenic transformation of marine diatoms into MFI-type aluminosilicate catalytic interfaces for selective etherification

Nadia Tuada Afnan, [a] Putri Ayunita Azahra,[a] Novi Syahra Almunadya,[a] Amila Laelalugina, [a] Rino R. Mukti, [bc] Grandprix T. M. Kadja, [bcd] Yanti Rachmayanti, [a] Daquan Zhang, [e] Aijie Liu, [ef] Zeily Nurachman, [a] Didin Mujahidin *[bgh] and Rindia M. Putri *[ab]

The biosilica of marine diatoms presents a sustainable and architecturally unique platform for the development of catalytic materials through transformation into aluminosilicate. However, previous studies have predominantly employed fossilized diatomite as a silica source instead of renewable diatom cultures. Furthermore, the catalytic activities have primarily been limited to catalytic cracking and pyrolysis, without demonstrating synthesis applications. In this work, we investigated the biogenic transformation of *Cyclotella striata* TBI marine diatom into MFI-type aluminosilicate, using tetrapropylammonium bromide as an organic structure-directing agent. The resulting materials exhibited porous architectures with an average pore radius of 5.96 nm and a surface area of 60.47 m^2 g^{-1}. Spectroscopic and microscopic analyses confirmed the formation of polycrystalline MFI-type frameworks with accessible Brønsted acid sites (0.6419 mmol g^{-1} catalyst). Catalytic etherification of ethanol with *tert*-butanol exhibited complete selectivity toward ethyl *tert*-butyl ether (ETBE) without detectable side products, achieving a turnover number of 16.4 mmol ETBE per mol active site. Only the aluminium-incorporated materials were catalytically active for etherification, thus highlighting the role of the engineered aluminosilicate interface in promoting selective reactivity. These findings establish a renewable biomass-to-catalyst pathway for fabricating functional catalytic interfaces in green fuel synthesis.

Received 3rd August 2025,
Accepted 24th September 2025

DOI: 10.1039/d5lf00224a

rsc.li/RSCApplInter

Introduction

Interfacial design plays a critical role in enabling sustainable acid-catalysed transformations, particularly in systems requiring high selectivity, such as the etherification reactions used to produce cleaner fuel oxygenates. Among these, ethyl *tert*-butyl ether (ETBE) has emerged as a greener bio-additive due to its high-octane number and cleaner combustion profile.[1] However, current ETBE production still relies heavily on synthetic catalysts such as ion-exchange resins and petroleum-derived zeolites, which present sustainability and disposal challenges.[2–5] As a result, efforts have increasingly focused on developing renewable catalytic materials that integrate structural tunability with interfacial functionality. Achieving such systems requires not only sustainable precursors but also precise control over pore architecture and the spatial accessibility of active sites to ensure high selectivity in etherification reactions.

In light of such challenges, marine diatoms provide a renewable, biogenic silica source that can be transformed into functional catalytic materials. Diatoms, a major class of microalgae, produce intricately patterned silica shells (so-called frustules) featuring hierarchical porosity,[6,7] high surface area,[8] and mechanical robustness.[9] These structural characteristics enable diatom biosilica to effectively support various catalytic species, including metal nanoparticles (*e.g.*, Au, Ag, Pd, and Pt), metal oxides like TiO_2, and various enzymes.[10–14] Accordingly, diatom biosilica has been widely

[a] *Biochemistry and Biomolecular Engineering Research Division, Faculty of Mathematics and Natural Sciences, Institut Teknologi Bandung, Jalan Ganesha No. 10, Bandung 40132, Indonesia. E-mail: rindia.m.putri@itb.ac.id*
[b] *Research Center for Nanosciences and Nanotechnology, Institut Teknologi Bandung, Jalan Ganesha No. 10, Bandung 40132, Indonesia*
[c] *Division of Inorganic and Physical Chemistry, Faculty of Mathematics and Natural Sciences, Institut Teknologi Bandung, Jalan Ganesha No. 10, Bandung 40132, Indonesia*
[d] *Center for Catalysis and Reaction Engineering, Institut Teknologi Bandung, Jalan Ganesha No. 10, Bandung 40132, Indonesia*
[e] *Fujian Provincial Key Laboratory of Innovative Drug Target Research, School of Pharmaceutical Sciences, Xiamen University, Xiamen 361102, China*
[f] *Shenzhen Research Institute of Xiamen University, Shenzhen 518057, China*
[g] *Organic Chemistry Division, Faculty of Mathematics and Natural Sciences, Institut Teknologi Bandung, Jalan Ganesha No. 10, Bandung 40132, Indonesia. E-mail: d.mujahidin@itb.ac.id*
[h] *Research Center on New and Renewable Energy, Institut Teknologi Bandung, Bandung, 40132, Indonesia*

employed as a support in catalytic transformations such as photocatalytic degradation, hydrogenation, oxidation, and cross-coupling reactions.[15–17] Beyond catalysis, its unique architecture has been harnessed for applications in drug delivery,[18] implant materials,[19,20] molecular sieves, and chromatography,[21–23] as well as environmental remediation.[24] However, in many of these examples, the biosilica primarily serves as a passive scaffold.

A sustainable approach for transforming diatom biosilica from a passive support into a functionally active material involves the chemical conversion of its amorphous surface into a crystalline aluminosilicate interface.[25–27] Incorporating aluminium into the silica framework introduces Brønsted acid sites, resulting in catalytic interfaces for reactions such as etherification. Nevertheless, previous efforts have predominantly relied on fossilized diatomite as a raw silica source instead of using renewable diatom cultures.[28–30] Furthermore, these fossil-derived aluminosilicates have primarily been tested as additives in catalytic cracking or plastic pyrolysis,[31,32] without demonstrating synthesis applications. To our knowledge, the design of a diatom-derived aluminosilicate and its application as a selective catalyst for ETBE synthesis has not been previously investigated.

In this work, we report the synthesis of a biogenic aluminosilicate catalyst from the biosilica of laboratory-cultivated *Cyclotella striata* TBI marine diatom and investigate its performance in selective etherification.[33] We show that a hydrothermal treatment using an organic structure-directing agent could transform the amorphous diatom biosilica into a polycrystalline material with a well-defined MFI-type framework. Notably, the resulting aluminosilicate exhibits a network of accessible acid sites at the newly formed interface, enabling catalytic activity for etherification. This work demonstrates the valorisation of renewable diatom biosilica into sustainable catalysts for green fuel synthesis.

Materials and methods

Cultivation of *Cyclotella striata* TBI marine diatom

Cyclotella striata TBI diatom cells (CS-Cell) were obtained from the collection of the Biochemistry and Biomolecular Engineering Laboratory of the Faculty of Mathematics and Natural Sciences, Institut Teknologi Bandung, Indonesia. CS-Cell cultures at an initial concentration of 2×10^8 cells per mL were cultivated in artificial seawater medium (22 ppt) containing 50 ppm Na_2EDTA, 3.3 mg L^{-1} $FeCl_3$, 10 mg L^{-1} TSP-36™ fertilizer (P_2O_5), 71 mg L^{-1} NPK™ fertilizer (KNO_3 and phosphate), and 45 mg L^{-1} sodium silicate (Na_2SiO_3) under a photoperiod of 12 : 12 h light:dark.[34]

Extraction of biosilica from marine diatom biomass

Biomass of CS-cell was harvested at the end of log phase using centrifugation (4500 rpm for 3 min at room temperature), followed by an acid treatment with 70% v/v HNO_3 and subsequent centrifugation (4000 rpm for 3 min at room temperature). The treatment was repeated until the supernatant was colourless. The pellet was washed 10 times with demineralized H_2O followed by an ethanol wash, dried at 80 °C for 24 h, and calcined in an electric furnace at 550 °C for 10 h. The white biosilica powder (called Sil-CS) was characterized by FTIR spectroscopy (Prestige 21 Shimadzu), SEM (Hitachi SU3500 at 10 kV), TEM (FEI Talos F200x), XRF spectroscopy (Bruker D8 Advanced), XRD (Bruker D8 Advanced), and TPD (ChemiSorb 2750 Micromeritics).

Transformation of diatom biosilica into aluminosilicate

Aluminosilicate (Al-Sil-CS) was synthesized by mixing Sil-CS, $Al(OH)_3$, TPABr, NaOH, and H_2O in a polypropylene bottle with a molar composition of $1 : x : 0.1 : 0.12 : 12$, with a varying value of x in the range of 0.01–1. The homogenized reaction mixture was heated in an oven at 90 °C for 96 h, followed by filtration of the precipitant, rinsing with deionized water, and drying at 100 °C for 4 h.[25] TPABr was removed by calcination at 550 °C for 6 h. All aluminosilicate samples were analysed using XRF, FTIR, SEM, TEM, and XRD.

Physicochemical characterization

FTIR analysis (Shimadzu Prestige 21) was performed on a solid sample using a KBr pellet with a 1 : 10 ratio of sample and KBr. For the SEM measurement (Hitachi SU3500), the sample was placed on a carbon surface under vacuum with an operating voltage of 10.0 kV. TEM imaging was performed at an operating voltage of 200 kV. XRD and XRF analyses were performed at 40 kV and 40 mA, respectively. NH_3-TPD analysis was performed by introducing a 5% NH_3/helium gas mixture using ChemiSorb 2750 Micromeritics at 100 °C for 30 minutes. He purging was carried out before and after the adsorption to replace excess NH_3 at 350 °C and 100 °C for 60 minutes, respectively. Desorption was carried out over a temperature range of 100–800 °C at a heating rate of 10 °C min^{-1} under helium flow.

Catalytic performance test for etherification reaction

To activate the catalyst, 1 g of aluminosilicate was acidified with 10 mL ammonium chloride (1 M) at 80 °C for 4 h. The activated aluminosilicate was then filtered, dried at 100 °C, and calcined at 550 °C for 4 h. Activation of aluminosilicate was repeated two times. The synthesis of ETBE was performed by mixing 1 mL ethanol p.a., 1 mL *tert*-butanol p.a., and 0.5 g of aluminosilicate in a closed Schlenk flask at 70 °C. The reaction mixture was stirred at 600 rpm for 4 h. The catalyst was removed from the reaction mixture by centrifugation at 12 000 rpm for 5 min (Thermoscientific SL16R), and the products were analysed by GC-MS using HP-5 column (Agilent 8890, Agilent 5977B GC/MSD) at an injector temperature of 100 °C, detector temperature of 260 °C, column temperature of 40–100 °C, and a flow rate of 11.8 mL min^{-1} at 100 kPa with HP-5 column. Mass analyses were performed at 230 °C. For post-catalysis

characterizations, the catalyst was collected and subjected to structural characterizations using SEM and XRD.

Results and discussion

Biomass productivity and sustainability

To evaluate the growth dynamics of the diatom, the cell density of *C. striata* TBI marine diatom was monitored daily for over 14 days in a modified seawater medium. Fig. 1a shows the growth profile of *C. striata* TBI diatom. Starting with a 2×10^8 cells mL^{-1}, the diatom cells (CS-cell) underwent an initial 2-day adaptation phase, followed by an exponential growth over the next 5 days. During the exponential phase, the culture rapidly turned yellowish brown with a specific growth rate (μ) of 0.22 d^{-1}, calculated based on the slope of Fig. 1b, with a doubling time of 3.15 days. Then, the cell density did not increase significantly from day 8 to 10, before decreasing rapidly afterwards. The biomass was harvested on day 10, with an average cell density of 12×10^8 cells per mL, which is equivalent to a biomass productivity of 194.42 mg L^{-1} d^{-1}.[34]

In terms of sustainability, the marine diatom cultures could be re-grown by introducing a fresh medium to restart the growth cycle. Moreover, a crucial factor for large-scale cultivation is the production cost of the biomass, including the cost of the growth medium. To address this, we adopted a modified medium formulation from Nurachman *et al.*,[34] which used commercial fertilizers as a low-cost replacement for the Walne medium. This modification reduced the overall production cost by ~84%, making it a far more economical and practical option for mass cultivation.

Biosilica characterization and morphological transformation to biogenic aluminosilicate

C. striata TBI biosilica (Sil-CS) was obtained from the biomass treated with HNO_3 washing and calcination, following reported procedure.[13,35,36] To conduct comprehensive characterization, the biosilica was analysed with SEM, HR-TEM, XRF, and SAED (Fig. 2a–d). Based on SEM image, biosilica of *C. striata* TBI exhibited a petri dish-like morphology with a diameter of 8–20 μm and a width of 1–8 μm (Fig. 2a). Furthermore, the Si K-α emission (1.74 keV) in the XRF spectrum corroborated the presence of Si (Fig. 2a). The architecture of *C. striata* TBI biosilica (Sil-CS), as revealed through high-resolution imaging (Fig. 2b), was intricate and featured hierarchical surface pores (Fig. 2c). The TEM cross-sectional view (Fig. 2b) unveiled a gradient in silica density, characterized by a denser outer layer and a porous network in the centre. Fig. 2c further features the interlayer macropores averaging 167 ± 12.24 nm in diameter, within which a secondary system of mesopores (up to 30 nm) was neatly embedded. SAED analysis (Fig. 2d) revealed the absence of diffraction patterns for *C. striata* TBI biosilica, indicating the amorphous nature of Sil-CS.

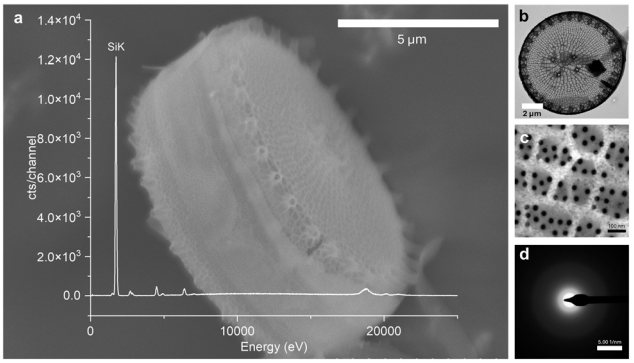

Fig. 2 Characteristics of *C. striata* TBI biosilica (Sil-CS). (a) SEM image of Sil-CS (scale = 5 μm) with overlaid XRF spectrum showing a dominant Si K-α emission, (b) TEM image of Sil-CS (scale = 2 μm), (c) TEM image of interlayer hierarchical pores on Sil-CS surface (scale = 100 nm), and (d) selected area electron diffraction (SAED) pattern of Sil-CS (scale = 100 nm).

Morphological and chemical transformation of *C. striata* TBI biosilica (Sil-CS) to biogenic aluminosilicates (Al-Sil-CS), as shown in Fig. 3, was accomplished through a hydrothermal conversion process, which utilized tetrapropylammonium bromide (TPABr) as an organic structure-directing agent (OSDA). This process successfully yielded well-defined, intergrowth particles as shown in Fig. 4a, with a characteristic Al K-α emission peak at 1.49 keV in the XRF spectrum (Fig. 4a). The crystallinity of Al-Sil-CS

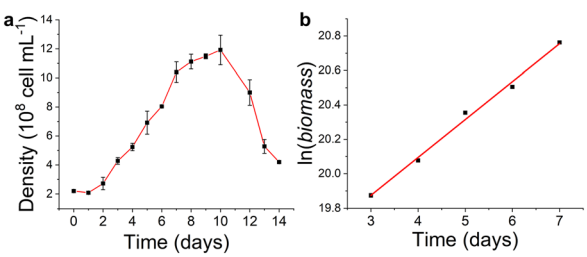

Fig. 1 Growth characteristics of *Cyclotella striata* TBI diatom. (a) Cell density over a 14-day cultivation period and (b) log-linear plot of biomass over time to calculate the doubling time during exponential growth.

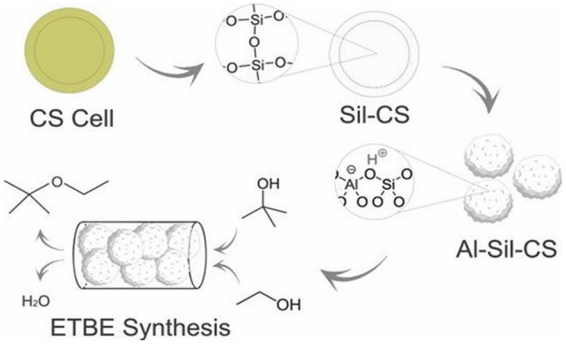

Fig. 3 Transformation of marine diatom cultures (CS-cell) into biosilica (Sil-CS) and subsequently into biogenic MFI-type aluminosilicate (Al-Sil-CS) for selective ETBE synthesis.

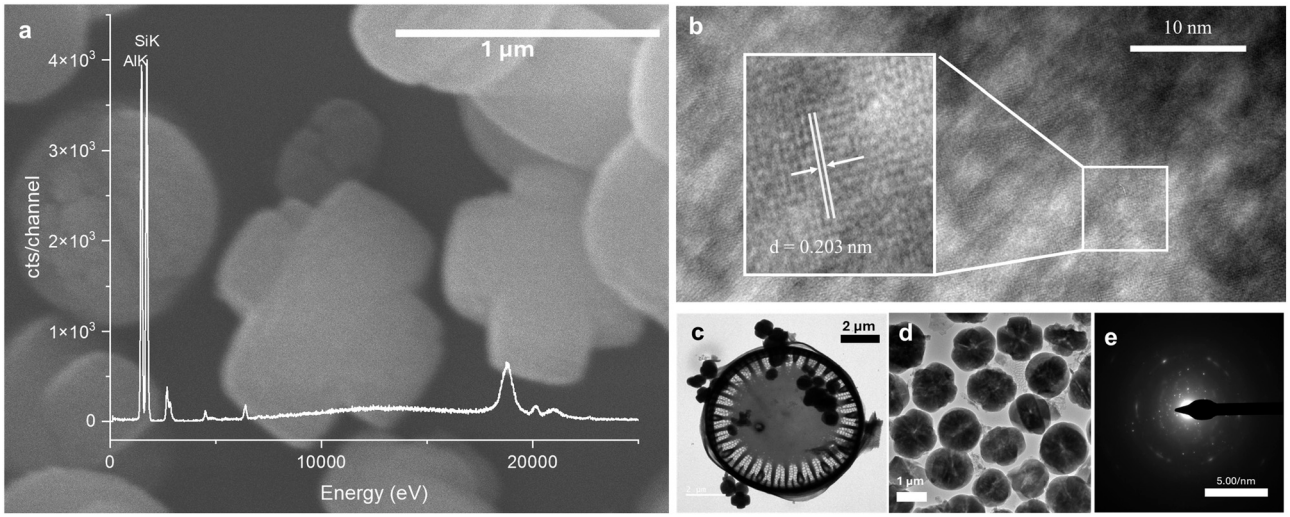

Fig. 4 Characteristics of biogenic aluminosilicates (Al-Sil-CS) from diatom biosilica. (a) SEM image (scale = 1 μm) with overlaid XRF spectrum showing Si and Al K-α emission peaks, (b) HR-TEM image with inset highlighting lattice fringes (d = 0.203 nm), confirming the crystalline structure, (c) TEM image showing smaller Al-Sil-CS particles in comparison to intact Sil-CS (scale = 2 μm) to visualize the structural transformation, (d) TEM image showing intergrown Al-Sil-CS (scale = 1 μm), and (e) selected area electron diffraction (SAED) pattern of the Al-Sil-CS (scale = 100 nm).

was evidenced by the presence of lattice fringes in HR-TEM image (Fig. 4b), with an interplanar spacing of approximately 0.203 nm. Fig. 4c shows a stark size-comparison of a much larger Sil-CS particle (of 13.6 μm in diameter) with the surrounding smaller Al-Sil-CS particles in vicinity. Intergrown Al-Sil-CS particles with the size of 700–900 nm are further shown in Fig. 4d. Furthermore, the corresponding SAED pattern in Fig. 4e also shows discrete diffraction spots, confirming the polycrystalline nature of Al-Sil-CS. In the Sil-CS to Al-Sil-CS transformation, tetrapropyl-ammonium cation (TPA^+) served as a molecular template for both the initial nucleation and the subsequent oriented attachment of the crystallites.[25,37]

Further structural comparison of Sil-CS and Al-Sil-CS was conducted using FTIR spectroscopy (Fig. 5a), XRD (Fig. 5b), and BET adsorption–desorption analyses (Fig. 5c and d). FTIR spectra of Sil-CS (Fig. 5a, red line) showed main vibration bands at 450 cm^{-1} and 1222 cm^{-1}, which are attributed to bending and asymmetric stretching modes of Si–O–Si, respectively. The incorporation of aluminium atoms into the silica network was confirmed by an additional vibration band at 555 cm^{-1}, which corresponds to the characteristic double 5MR vibration of MFI topology (Fig. 5a, black line).[38] Importantly, these characteristic vibrational bands remained consistent across all Al-Sil-CS samples without significant peak shifts, regardless of the Si/Al ratio (Fig. S1a). XRD diffractograms for Al-Sil-CS exhibited distinct peaks at 2θ = 7.8°, 8.0°, 22.8°, and 23.2°, which fit the characteristic patterns of an MFI framework (Fig. 5b), further confirming an MFI-type topography of Al-Sil-CS. The diffraction peaks were identical for all Al-Sil-CS materials at varying Si/Al ratio (Fig. S1b), indicating that the MFI-type structure was maintained across the range of Si/Al ratios examined in this study (Table 1).

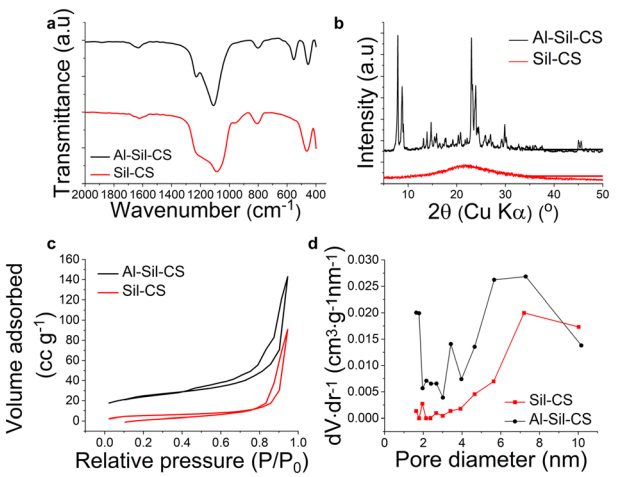

Fig. 5 Structural comparison of Sil-CS (red) and Al-Sil-CS (black). (a) FTIR spectra showing Si–O–Si vibrations and 5MR band in Al-Sil-CS, (b) XRD diffractograms indicating amorphous silica in Sil-CS and crystalline MFI-type framework in Al-Sil-CS, (c) N_2 adsorption–desorption isotherms showing increased surface area of Al-Sil-CS compared to Sil-CS, and (d) BJH pore size distribution of Sil-CS and Al-Sil-CS.

Table 1 Mol ratio of Si/Al in Al-Sil-CS samples determined using XRF

Initial ratio of Si/Al (mol)	Atomic%		Final ratio of Si/Al (mol)
	Si	Al	
1	71.72	28.28	2.53
10	90.75	9.25	9.81
30	97.15	2.85	34.08
60	98.02	1.98	49.50
80	98.59	1.41	69.92
100	99.11	0.89	111.36

The discrepancy between the initial and final Si/Al ratios (Table 1) can be attributed to the non-linear incorporation of aluminium during the biogenic zeolitisation process. In some cases, partial incorporation efficiency or subsequent leaching of Al species during hydrothermal treatment and template removal led to a higher final Si/Al ratio, reflecting lower Al content in the framework. In contrast, under strongly alkaline synthesis conditions, partial dissolution of silica could occur, effectively enriching the relative proportion of Al in the final solid and resulting in a lower Si/Al ratio. Such variations between feed and product composition are well-documented in zeolite syntheses from natural or non-conventional silica sources, in which framework incorporation of Al is less strictly controlled compared to synthetic precursors.[25,26]

The nitrogen physisorption isotherms (Fig. 5c) also revealed significant structural differences between Sil-CS and the derived Al-Sil-CS. While both materials exhibited a type-IV nitrogen adsorption–desorption isotherm, the hysteresis loop of Sil-CS appeared at a higher relative pressure (P/P_0 = 0.8), indicating the presence of relatively larger mesopores. BET analyses of Sil-CS resulted in a surface area of 30.14 $m^2\ g^{-1}$ and an average pore diameter of 15.2 nm. Meanwhile, the hysteresis loop for Al-Sil-CS (Fig. 5c) began at a lower relative pressure (P/P_0 = 0.6), with an average pore diameter of 5.96 nm and a twofold increase of surface area to 60.47 $m^2\ g^{-1}$. Altogether, spectroscopic, crystallographic, and physisorption analyses corroborated the transformation of biogenic amorphous Sil-CS to highly crystalline Al-Sil-CS particles.

Catalytic performance and selectivity

To determine the catalytic performance for etherification reaction, a mixture of ethanol and *tert*-butanol was reacted in the presence of Al-Sil-CS and monitored using GC-MS (Fig. 6). The formation of ethyl *tert*-butyl ether (ETBE) was confirmed by a distinct chromatographic peak at 2.33 min and *m*/*z* peaks at 57, 59, and 87 (Fig. 6a), matching ETBE fragmentation. Etherification of 17.1 mmol ethanol and 10.5 mmol *tert*-butanol produced an ETBE concentration of 10.54 mM, corresponding to 10.54 μmol ETBE g^{-1} catalyst in a 1 mL reaction mixture (Fig. 6b). A negative control using Sil-CS yielded negligible ETBE production (<2 mM ETBE g catalyst, Fig. 6b), confirming that the catalytic interface was formed due to aluminium incorporation. Notably, we did not observe any formation of side products, such as diethyl ether (DEE), based on analyses using GC-MS. Hence, a nearly complete selectivity (~100%) towards ETBE was achieved, with no detectable formation of side products.

The origin of the enhanced catalytic performance of Al-Sil-CS can be primarily attributed to the introduction of acid sites upon aluminium incorporation, as confirmed by NH_3-TPD analyses. As shown in Fig. S2, NH_3-TPD analyses

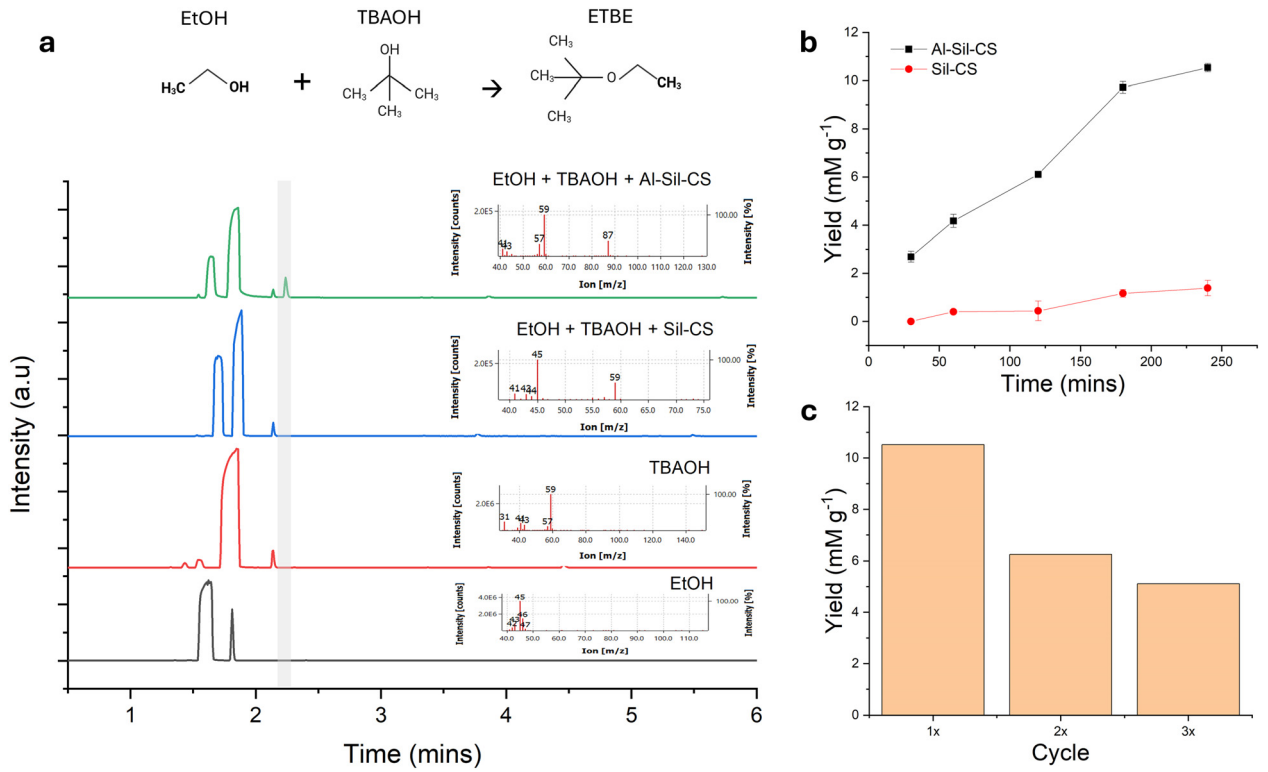

Fig. 6 Catalytic performance of Al-Sil-CS in ETBE synthesis. (a) GC-MS chromatogram highlighting ETBE peak (grey) and its corresponding mass fragments, (b) comparison of ETBE production yield using Al-Sil-CS (black) and Sil-CS (red), and (c) catalytic reusability of Al-Sil-CS over multiple cycles.

revealed that adjusting the aluminium content in Al-Sil-CS tuned the acidity of the catalyst. A lower Si/Al ratio led to a significant increase in the concentration of acid sites. The highest measured total acidity reached 0.6419 mmol g^{-1} and the desorption profile corroborated the presence of medium-strength acid sites. The role of acidity distribution has been highlighted in previous studies, showing that site strength and spatial arrangement could enhance activity and selectivity of MFI-type systems.[39,40] The turnover number (TON) and yield were calculated as 16.4 mmol ETBE per mol acid sites and 0.1%, respectively.

The nearly complete selectivity towards ETBE in this system likely reflects the nature and accessibility of the acid sites. Interfacial, surface-exposed acid site might have provided favourable orientation as well as proximity for ethanol and *tert*-butanol molecules. Previous studies have also shown that medium-strength Brønsted acid sites located at external surfaces could promote etherification over competing side reactions.[41,42] Moreover, the increase in surface area of Al-Sil-CS, compared to the parent Sil-CS, likely further improved surface accessibility, thereby supporting the observed catalytic behaviour. The combination of increased Brønsted acidity and enhanced surface area observed in NH_3-TPD and BET analyses, respectively, suggests the formation of interfacial "hot zones," defined in this context as regions within the catalyst architecture where accessible acid sites and mesopores may work synergistically to facilitate reactant adsorption and product formation.

Furthermore, catalyst recyclability was evaluated across three reaction cycles, revealing a significant deactivation trend with performance decreasing by ~40% in the second cycle and ~59% in the third (Fig. 6c). To rationalize the performance loss over cycles, post-reaction catalyst was characterized using SEM and XRD. SEM images of post-reaction catalyst showed that the particles became irregular in size and morphology (Fig. 7a and b), which is attributed to particle disintegration and aggregation.[43,44] The XRD pattern exhibited a marked decrease in the intensity of the characteristic ZSM-5 diffraction peaks (Fig. 7c), indicating partial loss of crystallinity and possible framework collapse. Hence, the partial deactivation over cycles, likely driven by structural failures,[45–47] is typical for early-stage aluminosilicates[48,49] and underscores the need for structural reinforcement to improve catalyst stability.[45–47,49,50]

The kinetic profile of the reaction was determined by fitting the experimental data to several models. As shown by a comparison of the coefficients of determination (R^2) in Fig. S3, zeroth-order kinetics provided the best fit (R^2 = 0.97). The linear plot for the zeroth-order kinetics is presented in Fig. 8. The adherence to zeroth-order kinetics suggests that the catalyst's active sites were saturated under the reaction conditions. Consequently, the surface reaction itself was likely the rate-determining step. Although no byproducts were detected (*i.e.*, ~100% selectivity), the catalyst exhibited low yield (0.1%) in comparison to synthetic counterparts (Table 2). Limited active site density and possible diffusion barrier likely contributed to the low overall turnover, which could be addressed in future studies through optimised hydrothermal synthesis or secondary templating strategies. Nevertheless, this work establishes a renewable, proof-of-concept route for directly converting living marine diatom biosilica into MFI-type aluminosilicate catalysts. Hence, this study lays the groundwork for the development of fully biogenic aluminosilicates for sustainable and selective etherification.

In future work, extending this catalytic system to other alcohols (*e.g.*, benzylic alcohols and higher linear alcohols) is essential to evaluate both scalability and broader

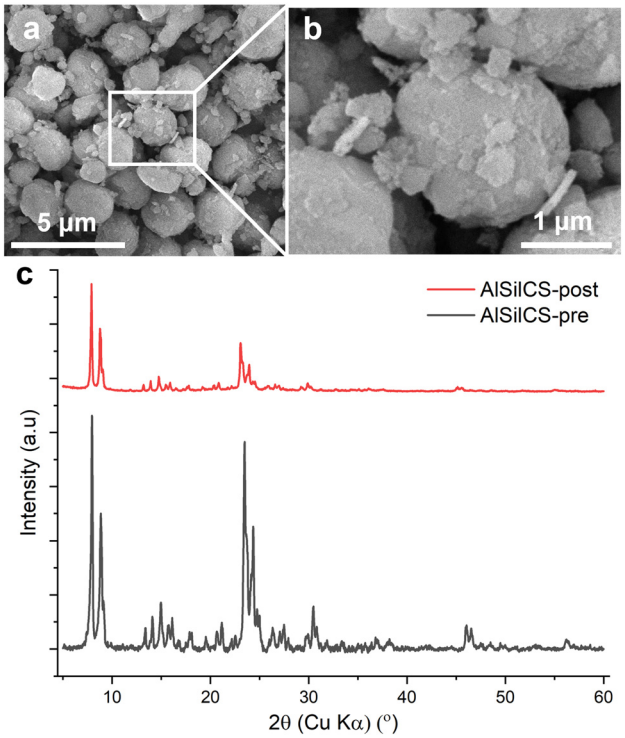

Fig. 7 Characterization of post-reaction catalyst. (a) SEM image of Al-Sil-CS post reaction (scale = 5 μm), (b) SEM image of Al-Sil-CS post reaction (scale = 1 μm), (c) an overlay of the X-ray diffractograms for the Al-Sil-CS catalyst, showing the structure pre and post reaction.

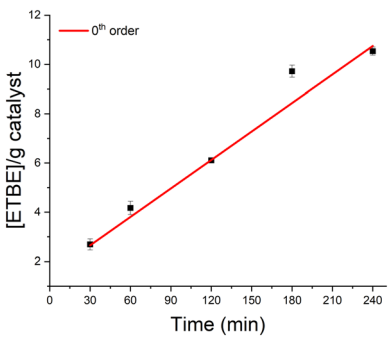

Fig. 8 Time-dependent yield of ETBE synthesis using Al-Sil-CS catalyst, fitted to zeroth-order kinetics (red line).

Table 2 Comparison of silica source (synthetic *vs.* biogenic) on ethyl *tert*-butyl ether (ETBE) production yield, conversion, and selectivity

Catalyst	Silica source	% conversion	% yield	% selectivity	Ref.
A-15	Synthetic	96.1–96.5	n.a.	n.a.	59
	Synthetic	70	n.a.	43	60
	Synthetic	n.a.	25	n.a.	53
	Synthetic	40–50	n.a.	~90	61
	Synthetic	n.a.	n.a.	100	53
A-35	Synthetic	85	n.a.	50	60
CT 124	Synthetic	~70	n.a.	~60	60
CT 151	Synthetic	~55	n.a.	~30	60
CT 275	Synthetic	~85	n.a.	~38	60
CT 175	Synthetic	~80	n.a.	~50	60
CT 145H	Synthetic	~80	n.a.	~60	60
US-Y	Synthetic	n.a.	8–11	n.a.	53
H-Mordenite	Synthetic	n.a.	8	n.a.	53
H-Omega	Synthetic	n.a.	5	n.a.	53
H-Beta	Synthetic	n.a.	19–34	n.a.	53
S-54	Synthetic	40–50	n.a.	~90	61
D-72	Synthetic	40–50	n.a.	~90	61
H-ZSM-5	Synthetic	n.a.	3–5	n.a.	53
	Synthetic	n.a.	20–30	n.a.	57
Al-Sil-CS	**Marine diatom biosilica**	**6**	**0.1**	**~100**	**This study**

applicability. Previous studies have shown that acid-functionalized porphyrin catalysts can promote etherification of benzyl and furfuryl alcohols under optimized conditions.[51,52] While these systems are structurally distinct from aluminosilicates, they demonstrate that tailored acid sites can enable etherification of bulkier alcohols. In addition, zeolitic aluminosilicates such as H-mordenite, beta, and Y-type frameworks have been reported in the etherification of bulkier substrates, including glycerol, benzyl alcohols, and C_4–C_8 alcohols, under optimized conditions.[53–58] Applying such investigations to our system will require careful consideration of steric effects and acidity requirements, which could further establish the versatility of biogenic aluminosilicates in selective etherification reactions.

Conclusions

We have demonstrated the direct transformation of marine diatom cultures into MFI-type aluminosilicate with distinct porosity and interfacial acidity suitable for etherification reactions. The acid-bearing catalytic interfaces enabled selective formation of ETBE from ethanol and *tert*-butanol without detectable byproducts. As the parent biosilica exhibited negligible catalytic activity, the origin of the catalytic interface in the biogenic aluminosilicate particles was attributed to their evolved surface architecture and introduction of acid sites. These findings highlight the potential of marine diatoms as renewable precursors for interfacial catalyst design and provide a foundation for future optimisation to improve catalytic efficiency.

Author contributions

Nadia Tuada Afnan: investigation and writing – original draft; Putri Ayunita Azahra: investigation; Novi Syahra Almunadya: investigation; Amila Laelalugina: investigation; Rino R. Mukti: methodology; Grandprix T. M. Kadja: methodology; Yanti Rachmayanti: resources; Daquan Zhang: investigation; Aijie Liu: investigation; Zeily Nurachman: conceptualization, supervision, resources; Didin Mujahidin: supervision and resources; Rindia M. Putri: conceptualization, supervision, resources, and writing – review & editing.

Conflicts of interest

The authors declare no conflict of interest.

Data availability

Supplementary information: characterization of Al-Sil-CS at varying Si/Al molar ratio, NH3-TPD profiles of Al-Sil-CS, and kinetic modelling of the catalytic reaction. See DOI: **https://doi.org/10.1039/D5LF00224A**.

All research data supporting the findings of this study have been made publicly available in the Figshare repository.

The datasets include raw data from the comprehensive characterization of biosilica derived from the *Cyclotella striata* TBI marine diatom (Sil-CS) and the biogenic aluminosilicates (Al-Sil-CS). The repositories include growth curve of marine diatom, EM images, SAED patterns, FTIR spectra, XRD patterns, XRF spectra, BET adsorption–desorption profiles and NH_3–TPD analyses. The repositories also contain raw data on catalytic performance, kinetic analyses, and product analyses using GC-MS, as well as post-catalysis characterizations. Each dataset is citable and accessible via a unique Digital Object Identifier (DOI), as detailed below.

The following is the list of DOIs:

1. Growth curve of marine diatom: **https://doi.org/10.6084/m9.figshare.29812628**.

2. SEM image of Sil-CS: **https://doi.org/10.6084/m9.figshare.29815259**.

3. SEM image of Al-Sil-CS: **https://doi.org/10.6084/m9.figshare.29815205**.

4. SAED patterns of Sil-CS: **https://doi.org/10.6084/m9.figshare.29813198**.

5. SAED patterns of Al-Sil-CS: **https://doi.org/10.6084/m9.figshare.29815274**.

6. FTIR spectra: **https://doi.org/10.6084/m9.figshare.29812229**.

7. XRD diffractogram: **https://doi.org/10.6084/m9.figshare.29812796**.

8. XRF spectra: **https://doi.org/10.6084/m9.figshare.29812928**.

9. BET adsorption–desorption curve: **https://doi.org/10.6084/m9.figshare.29811302**.

10. GC-MS chromatograms: **https://doi.org/10.6084/m9.figshare.29812451**.

11. Kinetics data: **https://doi.org/10.6084/m9.figshare.29811812**.

12. XRD diffractograms of Al-Sil-CS post-catalysis: **https://doi.org/10.6084/m9.figshare.30172819**.

13. SEM images of Al-Sil-CS post-catalysis: **https://doi.org/10.6084/m9.figshare.30172792**.

14. NH_3–TPD analyses of Al-Sil-CS: **https://doi.org/10.6084/m9.figshare.30172825**.

Acknowledgements

This work was supported by the Ministry of Higher Education, Science, and Technology through Pendidikan Magister menuju Doktor untuk Sarjana Unggulan program (PMDSU, No. 1343/D3/PG/2018 to N. T. A. and Z. N.), the Directorate for Research and Innovation (DRI), Institut Teknologi Bandung through Program Talenta Unggul Pusat Kajian Halal (PKH) 2025 DRI. PN-6-195-2025 (to N. T. A. and Z. N.), ITB research grant (Riset ITB) 2024 (No. 959/IT1.B07.1/TA.00/2024 to R. M. P.), National Nature Science Foundation of China (No. 22302164 to A. L.), and Shenzhen Science and Technology Innovation Commission, China (No. JCYJ20230807091311023 to A. L.). Some sentences in this manuscript were refined with the assistance of OpenAI's ChatGPT-4 to improve readability; all scientific content was developed and verified by the authors.

Notes and references

1 M. E. Bardin, A. M. T. A. El-Dein Hussin, P. A. Gushchin, V. A. Vinokurov and A. A. Burluka, *Energy Technol.*, 2014, **2**, 194–204.

2 J. F. Izquierdo, F. Cunill, M. Vila, M. Iborra and J. Tejero, *Ind. Eng. Chem. Res.*, 1994, **33**, 2830–2835.

3 S. F. Thornton, H. C. G. Nicholls, S. A. Rolfe, H. E. H. Mallinson and M. J. Spence, *J. Hazard. Mater.*, 2020, **391**, 122046.

4 Y. Le Digabel, S. Demanèche, Y. Benoit, F. Fayolle-Guichard and T. M. Vogel, *J. Hazard. Mater.*, 2014, **279**, 502–510.

5 G. Galán, M. Martín and I. E. Grossmann, *Comput.-Aided Chem. Eng.*, 2019, **47**, 391–396.

6 D. P. Medarević, D. Lošić and S. R. Ibrić, *Hem. Ind.*, 2016, **70**, 613–627.

7 D. Losic, R. J. Pillar, T. Dilger, J. G. Mitchell and N. H. Voelcker, *J. Porous Mater.*, 2007, **14**, 61–69.

8 D. Losic, J. G. Mitchell and N. H. Voelcker, *Adv. Mater.*, 2009, **21**, 2947–2958.

9 T. P. P. Coelho, B. P. Bezerra, J. R. Verza, A. P. Luz and M. R. Morelli, *Mater. Lett.*, 2023, **349**, 134784.

10 W. Xu, J. Su, J. Lin, J. Huang, M. Weng and Y. Min, *J. Energy Storage*, 2023, **72**, 108253.

11 M. Thakkar, Z. Wu, L. Wei and S. Mitra, *J. Colloid Interface Sci.*, 2015, **450**, 239–245.

12 I. Wojtczak, W. Brzozowska, Z. Bekissanova, G. Trykowski, P. Rybczyński, B. Ośmiałowski and M. Sprynskyy, *Colloids Surf., A*, 2025, **704**, 135463.

13 R. M. Putri, N. S. Almunadya, A. F. Amri, N. T. Afnan, Z. Nurachman, H. Devianto and W. H. Saputera, *ACS Omega*, 2022, **7**, 44047–44056.

14 V. Hegde, U. T. Uthappa, O. R. A. Swami, S. S. Han, H. Y. Jung, T. Altalhi and M. D. Kurkuri, *Mater. Today Commun.*, 2022, **32**, 103887.

15 O. R. Fonseca-Cervantes, A. Pérez-Larios, V. H. Romero Arellano, B. Sulbaran-Rangel and C. A. G. González, *Processes*, 2020, **8**, 1032.

16 C. Fischer, M. Adam, A. C. Mueller, E. Sperling, M. Wustmann, K. H. van Peé, S. Kaskel and E. Brunner, *ACS Omega*, 2016, **1**, 1253–1261.

17 M. Sprynskyy, P. Szczyglewska, I. Wojtczak, I. Nowak, A. Witkowski, B. Buszewski, A. Feliczak-Guzik and M. Martins, *Int. J. Mol. Sci.*, 2021, **22**, 6734.

18 U. T. Uthappa, V. Brahmkhatri, G. Sriram, H. Y. Jung, J. Yu, N. Kurkuri, T. M. Aminabhavi, T. Altalhi, G. M. Neelgund and M. D. Kurkuri, *J. Controlled Release*, 2018, **281**, 70–83.

19 A. D. Kashin, M. B. Sedelnikova, V. V. Chebodaeva, P. V. Uvarkin, N. A. Luginin, E. S. Dvilis, O. V. Kazmina, Y. P. Sharkeev, I. A. Khlusov, A. A. Miller and O. V. Bakina, *Ceram. Int.*, 2022, **48**, 28059–28071.

20 A. D. Kashin, M. B. Sedelnikova, P. V. Uvarkin, A. V. Ugodchikova, N. A. Luginin, Y. P. Sharkeev, M. A. Khimich and O. V. Bakina, *Biomimetics*, 2023, **8**, 280.

21 O. Hadjadj-Aoul, R. Belabbes, M. Belkadi and M. H. Guermouche, *Appl. Surf. Sci.*, 2005, **240**, 131–139.

22 M. Szumski, H. AlSaoud, I. Wojtczak, M. Sprynskyy, R. Gadzała-Kopciuch, S. Bocian, M. Dembek, M. Potrzebowski and B. Buszewski, *J. Chromatogr. A*, 2025, **1741**, 465603.

23 J. A. Kraai, G. L. Rorrer and A. X. Wang, *J. Chromatogr. A*, 2019, **1591**, 162–170.

24 G. Bayramoglu, A. Akbulut and M. Yakup Arica, *J. Hazard. Mater.*, 2013, **244–245**, 528–536.

25 G. T. M. Kadja, R. R. Mukti, Z. Liu, M. Rilyanti, Ismunandar, I. N. Marsih, M. Ogura, T. Wakihara and T. Okubo, *Microporous Mesoporous Mater.*, 2016, **226**, 344–352.

26 D. K. Yu, M. L. Fu, Y. H. Yuan, Y. B. Song, J. Y. Chen and Y. W. Fang, *J. Fuel Chem. Technol.*, 2016, **44**, 1363–1369.

27 M. Razavian, S. Fatemi and M. Komasi, *Mater. Res. Bull.*, 2015, **65**, 253–259.
28 M. W. Anderson, S. M. Holmes, N. Hanif and C. S. Cundy, *Angew. Chem., Int. Ed.*, 2000, **39**, 2707–2710.
29 P. Vinaches, A. J. Schwanke, C. W. Lopes, I. M. S. Souza, J. Villarroel-Rocha, K. Sapag and S. B. C. Pergher, *Molecules*, 2019, **24**, 1980.
30 M. Servatan, M. Ghadiri, M. K. Yazdi, M. Jouyandeh, G. Mahmodi, A. Samadi, P. Zarrintaj, S. Habibzadeh, M. R. Ganjali and M. R. Saeb, *Silicon*, 2021, **13**, 3461–3472.
31 X. Zhou, R. Wang, P. Wang, A. Zheng, M. Lou, Z. Wang, W. Zhao, Y. Song, H. Song and W. Lin, *Ind. Eng. Chem. Res.*, 2025, **64**, 8834–8846.
32 Y. Li, H. Sun, R. Feng, Y. Wang, F. Subhan, Z. Yan, Z. Zhang and Z. Liu, *Appl. Petrochem. Res.*, 2015, **5**, 347–353.
33 M. Song, C. Qiu, P. Ma, J. Zhong, Z. Zhang, W. Fang, W. Song, J. Fan and W. Lai, *Renewable Energy*, 2023, **212**, 468–477.
34 Z. Nurachman, Hartati, S. Anita, E. E. Anward, G. Novirani, B. Mangindaan, S. Gandasasmita, Y. M. Syah, L. M. G. Panggabean and G. Suantika, *Bioresour. Technol.*, 2012, **108**, 240–244.
35 Z. Y. Fakhrizal, F. I. Machmud, M. Y. Azis, R. M. Putri, R. T. Rosmalina and Z. Nurachman, *Int. J. Environ. Anal. Chem.*, 2025, 1–21.
36 R. M. Putri, D. Zhang, I. J. Manoela, H. T. Agustina, G. W. Patiung, A. Kono, D. Hardianti, J. X. Goh, Y. Rachmayanti, Z. Nurachman and A. Liu, *Langmuir*, 2025, **41**, 14062–14075.
37 A. H. Mukaromah, G. T. M. Kadja, R. R. Mukti, I. R. Pratama, M. A. Zulfikar and B. Buchari, *ITB J. Math. Fundam. Sci.*, 2016, **48**, 241–251.
38 D. I. Lashchenko, R. G. Kukushkin, I. G. Danilova, I. V. Yakovlev, O. A. Bulavchenko, A. P. Lyulyukin, V. O. Rodina and V. A. Yakovlev, *Mater. Today Chem.*, 2025, **46**, 102735.
39 H. Balcom, A. J. Hoffman, H. Locht and D. Hibbitts, *ACS Catal.*, 2023, **13**, 4470–4487.
40 A. J. Jones and E. Iglesia, *ACS Catal.*, 2015, **5**, 5741–5755.
41 N. V. Vlasenko and P. E. Strizhak, *J. Appl. Polym. Sci.*, 2022, **139**, 51926.
42 D. T. Hieu, H. Kosslick, M. Riaz, A. Schulz, A. Springer, M. Frank, C. Jaeger, N. T. M. Thu and L. T. Son, *Catalysts*, 2022, **12**, 253.
43 Q. Wu, H. Zou, Y. Han, L. Wu, S. Ma, L. A. Smillie, X. Su, Y. Chu, H. Deng, X. Mao, F. Zhu, D. Zhang, F. Liu, S. Shen, J. Zhao, L. Le Duan, A. Du, J. Chen and X. Yao, *Adv. Funct. Mater.*, 2025, e18284.
44 S. J. Park, J. W. Bae, G. I. Jung, K. S. Ha, K. W. Jun, Y. J. Lee and H. G. Park, *Appl. Catal., A*, 2012, **413–414**, 310–321.
45 M. Vares, A. Sari and F. Yaripour, *Fuel*, 2025, **383**, 133861.
46 F. L. Bleken, K. Barbera, F. Bonino, U. Olsbye, K. P. Lillerud, S. Bordiga, P. Beato, T. V. W. Janssens and S. Svelle, *J. Catal.*, 2013, **307**, 62–73.
47 Y. Jun, S. Lee, K. Lee and M. Choi, *Microporous Mesoporous Mater.*, 2017, **245**, 16–23.
48 E. Al-Shafei and Z. Shakor, *J. Anal. Appl. Pyrolysis*, 2024, **183**, 106830.
49 A. Yamaguchi, D. Jin, T. Ikeda, K. Sato, N. Hiyoshi, T. Hanaoka, F. Mizukami and M. Shirai, *Fuel Process. Technol.*, 2014, **126**, 343–349.
50 D. Padovan, A. Al-Nayili and C. Hammond, *Green Chem.*, 2017, **19**, 2846–2854.
51 K. J. Bhansali and P. R. Bhagat, *Fuel*, 2020, **278**, 118394.
52 V. S. Patil and P. R. Bhagat, *New J. Chem.*, 2025, **49**, 9721–9733.
53 F. Collignon and G. Poncelet, *J. Catal.*, 2001, **202**, 68–77.
54 P. M. Veiga, A. C. L. Gomes, C. D. O. Veloso and C. A. Henriques, *Mol. Catal.*, 2018, **458**, 261–271.
55 P. M. Veiga, A. C. L. Gomes, C. O. Veloso and C. A. Henriques, *Appl. Catal., A*, 2017, **548**, 2–15.
56 N. Ozbay, N. Oktar, G. Dogu and T. Dogu, *Top. Catal.*, 2013, **56**, 1790–1803.
57 R. Alcántara, E. Alcántara, L. Canoira, M. J. Franco, I. Martín and A. Navarro, *React. Kinet. Catal. Lett.*, 2000, **69**, 239–246.
58 N. Candu, M. Florea, S. M. Coman and V. I. Parvulescu, *Appl. Catal., A*, 2011, **393**, 206–214.
59 M. G. Sneesby, M. O. Tadé, R. Datta and T. N. Smith, *Ind. Eng. Chem. Res.*, 1997, **36**, 1855–1869.
60 M. Umar, D. Patel and B. Saha, *Chem. Eng. Sci.*, 2009, **64**, 4424–4432.
61 B. L. Yang, S. B. Yang and R. Q. Yao, *React. Funct. Polym.*, 2000, **44**, 167–175.